Sediment-generated noise and bed stress in a tidal channel

Christopher Bassett,[1] Jim Thomson,[2] and Brian Polagye[1]

Received 24 October 2012; revised 13 March 2013; accepted 20 March 2013.

[1] Tidally driven currents and bed stresses can result in noise generated by moving sediments. At a site in Admiralty Inlet, Puget Sound, Washington State (USA), peak bed stresses exceed 20 Pa. Significant increases in noise levels are attributed to mobilized sediments at frequencies from 4–30 kHz with more modest increases noted from 1–4 kHz. Sediment-generated noise during strong currents masks background noise from other sources, including vessel traffic. Inversions of the acoustic spectra for equivalent grain sizes are consistent with qualitative data of the seabed composition. Bed stress calculations using log layer, Reynolds stress, and inertial dissipation techniques generally agree well and are used to estimate the shear stresses at which noise levels increase for different grain sizes. Regressions of the acoustic intensity versus near-bed hydrodynamic power demonstrate that noise levels are highly predictable above a critical threshold despite the scatter introduced by the localized nature of mobilization events.

Citation: Bassett, C., J. Thomson, and B. Polagye (2013), Sediment-generated noise and bed stress in a tidal channel, *J. Geophys. Res. Oceans*, *118*, doi:10.1002/jgrc.20169.

1. Introduction

[2] Sources of ambient noise in the ocean have been the focus of numerous scientific studies dating back to World War II. Among the most commonly identified sources of ambient noise are shipping traffic [*Wenz*, 1962; *Greene and Moore*, 1995], weather [*Wenz*, 1962; *Nystuen and Selsor*, 1997; *Ma et al.*, 2005], biological sources [*Greene and Moore*, 1995], and molecular agitation [*Mellen*, 1952]. A more limited body of research identifies the motion of different sized sediment grains due to strong currents or surface waves as an ambient noise source [*Voglis and Cook*, 1970; *Harden Jones and Mitson*, 1982; *Thorne*, 1986b; *Thorne et al.*, 1989; *Thorne*, 1990; *Mason et al.*, 2007]. Noise generated by mobilized sediments is referred to as sediment-generated noise. The frequency of sound produced by particle collisions can be related to the size of the mobile particles [*Thorne*, 1986a]. Given that incipient motion of particles is driven by hydrodynamic conditions, for water depths on the order of 100 m, noise from coarse-grained sediments is only likely to be produced by high-current environments (e.g., current velocities >2 m s^{-1}), restricting the geographic range in which this sound makes a significant contribution to ambient noise levels. In shallower water (i.e., depths on the order of 10 m or less), noise from the resuspension and transport of sediments by surface waves and wave-current interactions is also possible and more likely to be observed over a broader geographic range.

[3] A lack of data identifying sediment-generated noise as an important ambient noise source in a range of coastal environments represents a data gap with implications for passive acoustic studies of marine species that inhabit such areas (i.e., SNR for detection, classification, and localization algorithms), and for monitoring anthropogenic noise in these areas. For example, tidal energy projects are in various stages of development in coastal waters of the United States, Canada, the United Kingdom, Ireland, and South Korea. There are significant knowledge gaps with respect to possible environmental impacts of tidal energy projects [*Polagye et al.*, 2011]. Sites suitable for tidal energy experience strong currents (>2 m s^{-1}) that, depending on bottom type, could mobilize sediments. Sediment-generated noise needs to be understood to design effective characterization and monitoring studies of the sound produced by tidal energy projects and its effects on marine mammals.

[4] The conditions under which incipient motion of particles occurs has long been an active research area. *Shields'* [1936] commonly cited work noted that lack of similarity between experiments and a lack of understanding of natural processes affecting motion of the bed were the two most important difficulties faced in developing relationships between hydrodynamic conditions and bed load transport. To address these problems, controlled laboratory experiments were performed on bed types consisting of homogenous grain sizes with different densities. Results were presented in terms of dimensionless parameters to generalize the results. The non-dimensionalized tractive forces, called the Shields parameter (Θ_b), were described as

$$\Theta_b = \frac{\tau_b}{(\rho_s - \rho)gD}, \quad (1)$$

Additional supporting information may be found in the online version of this article.

[1]Department of Mechanical Engineering, University of Washington, Seattle, Washington, USA.

[2]Applied Physics Laboratory, University of Washington, Seattle, Washington, USA.

Corresponding author: C. Bassett, Department of Mechanical Engineering, University of Washington, Stevens Way, Box 352600, Seattle, WA 98103, USA. (cbassett@uw.edu)

©2013. American Geophysical Union. All Rights Reserved.
2169-9275/13/10.1002/jgrc.20169

where τ_b is the bed stress, ρ_s is the density of the sediment, ρ is the density of the water, g is gravity, and D is the diameter of the sediment grain. Results were presented against the grain Reynolds number (Re_*) using the shear velocity (u_*) as the characteristic velocity scale. For a particular flow regime (i.e., Re_*), once the Shields parameter exceeded a critical value, incipient motion occurred. The empirical relationships identified by Shields have been revisited numerous times in the literature. For example, *Miller et al.* [1977] and the references therein include relationships for incipient motion of coarse-grained sediments. Miller *et al.* noted that predictions of incipient motion are difficult in complex natural environments due to turbulence, bed forms, and grain size distributions.

[5] Incipient motion of particles is often presented as a function of the mean shear stress or shear velocity. Field data [*Heathershaw and Thorne*, 1985], experimental results [*Diplas et al.*, 2008], and numerical analysis [*Lee and Balachandar*, 2012] have highlighted how drag forces and turbulence can affect critical shear stresses. Unlike *Shields* [1936], these studies suggest that drag forces on individual grains, rather than overall bed stresses, are more appropriate for predicting incipient motion. Instantaneous forces associated with turbulent fluctuations can mobilize grains, even when mean shear stresses are below critical values. Instantaneous near-bed forces are, however, difficult to quantify in high-energy field environments.

[6] Once sediments are mobilized, there are two mechanisms by which sound is generated: bed load and saltation [*Mason et al.*, 2007]. Bed load is the sustained motion of particles as a result of intergranular forcing and saltation is the partial entrainment and resettlement of grains that are too large for sustained motion across the seabed. Regardless of the type of motion, sound is generated as a result of collisions between individual particles.

[7] Laboratory experiments using artificial and real sediments have demonstrated that the spectral structure of sediment-generated noise is related to the material properties and size of the particles by

$$f_r \approx 0.182 \left[\frac{E}{\rho(1-\sigma^2)} \right]^{0.4} \left(\frac{g^{0.1}}{D^{0.9}} \right), \tag{2}$$

where f_r is the resonant frequency, E is Young's modulus, σ is Poisson's ratio, ρ is the particle density, g is the gravitational acceleration, and D the particle diameter [*Thorne*, 1985, 1986a]. By applying the material properties, the centroid frequency of sediment-generated noise becomes a function of only the grain diameter. *Thorne* [1986a] related the frequency to the grain diameter according to

$$f_c = \frac{192}{D^{0.9}}, \tag{3}$$

which showed good agreement with laboratory measurements. It was also found that the expression for spherical particles could be applied with good agreement to non-spherical particles [*Thorne*, 1986a].

[8] As a result of agreement between radiated noise from non-spherical particles and expected theoretical resonant frequencies of spherical particles, equation (3) can be inverted to solve for the size of arbitrarily shaped agitated sediment grains. *Thorne* [1986a] also applied the inversion of the expected resonant frequency for equivalent particle diameter (equation (3)) to field measurements of sediment-generated noise. The frequencies attributed to noise from moving sediments agreed with video analysis and sediment grabs at the site. Further attempts to apply acoustic data to accurately recreate the particle size distribution of the bed were less successful. They did, however, demonstrate that such estimates can capture the principal components of mobile particles [*Thorne*, 1986a]. Subsequent research applied the results to noise from bed load transport in West Solent, United Kingdom. At this site, a linear relationship between mobilized mass and recorded sound intensity was verified using a hydrophone and video analysis [*Thorne*, 1986b; *Thorne et al.*, 1989; *Williams et al.*, 1989; *Thorne*, 1990]. *Mason et al.* [2007] successfully applied the inversion method to a full-scale shingle transport experiment.

[9] This paper presents data collected from a tidal channel in which peak currents exceed 3 m s^{-1}. The results and discussion address three distinct but interrelated topics: the hydrodynamic conditions that give rise to bed load transport, the spectral content of sediment-generated noise, and the relationship of sediment-generated noise given prevailing hydrodynamic conditions. Section 2 outlines concepts critical to the interpretation of the results, data acquisition, and processing methods for each area of analysis. In section 3, the results are presented and used to investigate the relationship of sediment-generated noise to near-bed currents. Questions raised by the findings of this study, comparisons to previously published results, and transferability of results to other sites are discussed in section 4.

2. Methods

2.1. Site Description

[10] The study site is located in Admiralty Inlet, Puget Sound, Washington (USA). The majority of the tidal exchange between Puget Sound and the Strait of Juan de Fuca occurs in Admiralty Inlet, resulting in currents in excess of 3.0 m s^{-1} [*Polagye and Thomson*, 2013]. A map of Admiralty Inlet, Puget Sound, and the bathymetry are included in Figure 1.

[11] Classification of the seabed at the site is difficult due to the water depth (>50 m), lack of ambient light, and strong currents. Acoustic profiling undertaken in 2009 [*Snohomish PUD*, 2012] indicated a hard substrate, but could not provide a more accurate classification. Transects by a remotely operated vehicle (ROV) [*Greene*, 2011, an appendix to *Snohomish PUD* [2012]], are the most comprehensive data set currently available. Grain size distributions in the ROV survey were determined using ranging lasers separated by 10 cm on the ROV housing. Grain size classification was made based on a modified Wentworth scale where D is the characteristic diameter of the grain [*Wentworth*, 1922]. The reported bottom types included a combination of small boulders (D = 25.6–40.0 cm), cobbles (D = 6.4–25.6 cm), pebbles (D = 3.2–6.4 cm), gravel (D = 0.2–3.2 cm), and coarse sand (D = 0.05–0.2 cm). *Greene* [2011] reports two dominant substrate types within the immediate vicinity (O(100 m)) of the study site: a soft, unconsolidated bimodal distribution of pebble and gravel likely to be mobilized during strong currents, and a mix of cobble (35–50%), pebbles (<35%), and small boulders. Small boulders and

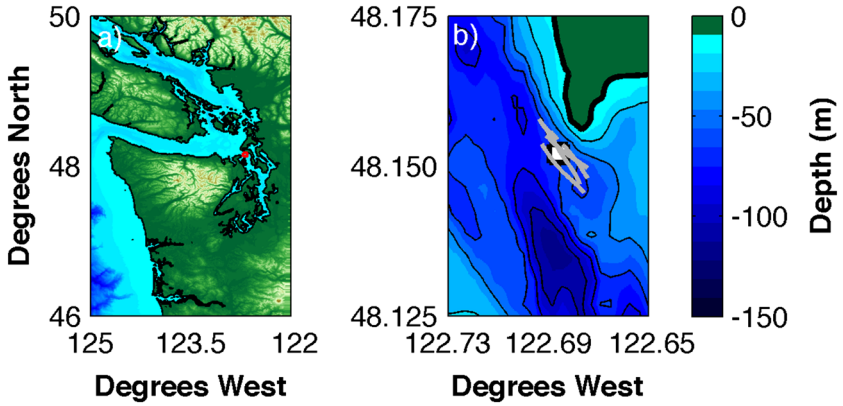

Figure 1. (a) A map of the Salish Sea. The red box highlights northern Admiralty Inlet. (b) A map of northern Admiralty Inlet, Puget Sound, and the deployment site. The deployments are represented by a white square (the Feb 2011 and June–Sept 2012 locations are indistinguishable at this scale) and gray lines (Oct 2011 drifts).

cobbles were typically well rounded and moderately to heavily encrusted with sponges, bryozoans, barnacles, tube worms, and algae, suggesting these substrates to be stationary [*Greene*, 2011]. Finer-grain constituents have been largely winnowed from the surface pavement. Where pebbles, gravel, and coarse sand were reported, they were unencrusted. Farther from the locations where instrumentation packages were deployed, in areas with weaker currents, pebbles were encrusted. In general, the substrate was unconsolidated and smaller constituents were easily moved by the ROV.

2.2. Data Collection

[12] Oceanographic and acoustics measurements were obtained using a combination of autonomous instrumentation packages built around Sea Spider tripods (Oceanscience, Ltd.) and ship-based cabled instruments. Three primary deployments were used in data analysis and two additional deployments were used to obtain supplementary information. All deployments were in northeastern Admiralty Inlet, near Whidbey Island. A list of the deployments, locations, and instruments used in the analysis are included in Table 1. The relationship between noise levels and hydrodynamics are based on the February 2011 deployment (tripod at depth of 55 m). October 2011 (shipboard cabled drifts) data were used to assess the directionality and June–September 2012 data (tripod at depth of 54 m) were used to assess the intermittency and stationarity of sediment-generated noise.

2.2.1. Acoustic Wave and Current Profiler

[13] A 1 MHz Nortek Acoustic Wave and Current profiler (AWAC) was used to measure currents from 1.05 to 26.05 m above the seabed. The AWAC profiled the water column in 0.5 meter bins at a frequency of 1 Hz during the February 2011 deployment. Mean current magnitude and direction were calculated using 5 min ensembles. As shown in *Thomson et al.* [2012], this ensemble period filters out the majority of turbulence. The standard error for a single ping measurement, also referred to as "Doppler noise," was $\sigma_u = 0.224$ m s^{-1}. The uncertainty in each velocity bin as a function of σ_u and the number of raw pings, N, in the ensemble is $\overline{u} \pm \frac{\sigma_u}{\sqrt{N}}$ [*Brumley et al.*, 1991]. For 5 min ensembles, the resulting uncertainty was 0.013 m s^{-1}, a value two orders of magnitude smaller than observed maximum non-turbulent currents (i.e., mean currents).

[14] Current profiles obtained using the AWAC during the August–November 2011 deployment were used to determine current velocities during shipboard drift surveys on 25 October 2011. Each profile was based on 30 sec averages obtained every 60 sec in 1 meter spatial bins. The resulting uncertainty in the currents was 0.045 m s^{-1}.

2.2.2. Acoustic Doppler Current Profiler

[15] A 470 kHz Nortek Continental Acoustic Doppler Current Profiler (ADCP) was used to measure currents from 1.69 to 49.69 m above the seabed in 1 m bins during the June–September 2012 deployment. Mean current magnitude and direction were calculated using 1 min ensembles. Linear interpolations of the February 2011 data were used to calculate a scalar factor to convert the velocity in the lowest bin of the June–September 2012 data (1.69 m) to the expected near-bed velocity at the same height as the February 2011 data (1.05 m). Current profiles were used only to approximate near-bed currents for the purposes of studying the intermittency and stationarity of sediment-generated noise during strong currents.

Table 1. Deployments, Locations, and Instrument Packages Used in this Study

Deployments	Location	Instruments	Purpose
11–21 Feb 2011	48 09.120°N, 122 41.152°W	ADV, AWAC, Hydrophones (×2)	Bed stress and ambient noise
9 Aug 2011	48 09.124°N, 122 41.195°W	GoPro Hero (×2), Dive lights (×4)	Video of seabed
10 Aug–14 Nov 2011	48 9.148°N, 122 41.305°W	AWAC	Current profiles during drift survey
25 Oct 2011	Drifts	Cabled hydrophones (×2)	Ambient noise
		Pressure logger	Hydrophone depth
12 June–19 Sept 2012	48 09.172°N, 122 41.171°W	ADCP, Hydrophone	Current profiles and ambient noise

2.2.3. Acoustic Doppler Velocimeter

[16] Point velocity measurements were acquired by a 6 MHz Nortek Vector Acoustic Doppler Velocimeter (ADV) during the February 2011 deployment. The ADV, deployed 1 m above the seabed, sampled the three components of velocity at 32 Hz for 256 sec every 10 min. For each burst sample (8192 points), data were projected on to the principal axis and reviewed for quality. Despiking of the projected velocity components was accomplished using the phase-space method [*Goring and Nikora*, 2002; *Mori et al.*, 2007] and the Matlab (www.mathworks.com) toolbox developed by *Mori et al.* [2007].

2.2.4. Hydrophone Data

[17] The standalone acoustic recording system on the tripod consisted of a Loggerhead Instruments DSG data acquisition and storage system with a Hi-Tech hydrophone (HTI-96-MIN) deployed 1 m above the seabed. The hydrophone, when accounting for the internal preamplifier, had an effective sensitivity of –165.9 dB μPa V^{-1}. The frequency response of the hydrophone and data acquisition system was approximately flat over the frequency range included in this study (1–30 kHz). Digitized 16-bit data were written to an SD card (32 or 128 GB) contained in the hydrophone pressure case. The data used for relating hydrodynamic and acoustic measurements were obtained from 11 February to 21 February 2011. During this deployment, the hydrophones recorded at 80 kHz for 10 sec at the top of every minute, a 17% duty-cycle motivated by memory limitations (32 GB SD card).

[18] A Loggerhead Instruments DSG equipped a larger flash memory card (128 GB) was deployed on a tripod from 12 June to 19 September 2012. During this period, the hydrophone sampled at 80 kHz for 55 sec at the top of every minute from 02:00–07:00. These hours were chosen due to relatively low levels of shipping and ferry traffic overnight [*Bassett et al.*, 2012]. The data were saved as 55 sec recordings for further processing. These data were used to assess the intermittence and stationarity of sediment-generated noise at the site (section 4.2).

[19] Increased noise levels at frequencies consistent with sediment-generated noise suggested the seabed as the noise source. To further test this hypothesis, measurements of the directionality were opportunistically carried out on 25 October 2011 during strong spring tidal currents, favorable weather conditions (no precipitation and sea state 0 to 1), and the cancelation of the ferry service that traverses the inlet. A ship-based cabled array consisted of two Cetacean Instruments CR55XS hydrophones with 10x internal preamplifiers separated by 10 cm (one-half of an acoustic wavelength at 7.5 kHz). The hydrophones were connected to an IOtech Personal Daq 3000 (16-bit, 1 MHz sampling rate) and to a laptop operating on battery storage to reduce 60 Hz electrical noise. Data were acquired continuously at 400 kHz while drifting through the site (no engines, generators, or active acoustics devices) on the R/V Inferno, a 24' research vessel owned by the Applied Physics Laboratory at the University of Washington. The sampling uncertainty for each channel of the data acquisition system was approximately 1 μs, 130 times shorter than the wave period at 7.5 kHz. After each drift, the vessel was repositioned more than 500 m upstream of the study area and the drift repeated. Six drifts were carried out from early in the ebb ($\overline{u}$ < 1 m s^{-1}) to past the peak ($\overline{u}$ > 3 m s^{-1}). Current velocity was assessed post hoc using profiles collected by the AWAC deployed on the tripod from August to November 2011. The hydrophone cables were mated to a "hairy rope" fairing to reduce cabled strum. Sash weights attached below the hydrophones were used to limit line angle. To minimize the transmission of boat motion to the hydrophones, the cables were deployed with slack leading to an isolation float tethered to the vessel using a 0.7 m shock cord. A HOBO U20 pressure logger (0.2 Hz sample rate) was deployed 40 cm below the hydrophones to record their depth. The intended deployment depth was approximately 40 m, between 5 and 15 m above the seabed.

2.2.5. Seabed Video

[20] On 9 August 2011, two GoPro Hero high definition video cameras were deployed on a mooring at the site. The cameras were deployed 65 cm above the bed with 55° incidence angles. The cameras were deployed facing opposite directions. The field of view was 170° for each camera. Two dive lights (one Hollis LED5 and one IKELITE PCm) were deployed next to each camera to provide artificial light in the center of the field of view. Due to battery life, the cameras were only able to record video for 4 h starting with the slack tide deployment. Video was obtained continuously throughout the 4 h period at 30 frames per second until the batteries failed, a period during which near-bed currents exceeded 1 m s^{-1}. The video was manually reviewed for mobilization events, including still frame tracking of individual grains.

2.3. Hydrodynamics Data Processing

[21] There are three methods commonly used to estimate shear stress at the seabed. Those methods make use of the log layer velocity profile, the inertial dissipation of turbulent kinetic energy, and the turbulent Reynolds stresses. The different methods, each discussed in detail below, can be compared to each other by a drag law according to

$$\tau_b = \rho u_*^2 = C_D \rho \, |\overline{u}| \, \overline{u}, \tag{4}$$

where τ_b is the bed stress, u_* is the friction velocity, C_D is the bottom drag coefficient, ρ is the fluid density, and $\overline{u}$ is the mean velocity.

2.3.1. Log Layer Velocity Profiles

[22] In a fully developed turbulent flow, the law of the wall provides a self-similar solution relating the mean velocity to the log of the distance from the wall, or in this case, the seabed. In this layer, the vertical gradient of the along-channel velocity (u) is defined by

$$\frac{\partial u}{\partial z} = \frac{u_*}{\kappa z}, \tag{5}$$

where u_* is the shear velocity, κ is the von Karmen constant, and z is the distance from the seabed.

[23] Integration of equation (5) yields the logarithmic boundary layer profile

$$u(z) = \frac{u_*}{\kappa} \, ln\left(\frac{z}{z_o}\right), \tag{6}$$

where the limits of integration are zero velocity at the roughness height (z_0), and the mean velocity is equal to u at height z. This methodology has been widely used and statistical considerations of the profile accuracy under different hydrodynamic conditions have received rigorous treatment

[*Heathershaw*, 1979; *Gross and Nowell*, 1983; *Grant et al.*, 1984; *Green*, 1992; *Lueck and Lu*, 1997].

[24] The uncertainty of the shear velocity is related to the log layer fit by

$$\Delta u_* = t_{\alpha/2,n-2}\left[\frac{1}{n-2}\left(\frac{1-R^2}{R^2}\right)\right]^{1/2}, \quad (7)$$

where $t_{\alpha/2,n-2}$ is the Student's t-statistic for a confidence level α with n degrees of freedom and R^2 is the coefficient of determination [*Gross and Nowell*, 1983]. Since the uncertainty in density is negligible (CTD measurements using a Seabird 16plus recorded density variations of less than 2 kg m^{-3}, relative to a nominal value of 1024 kg m^{-3} during the February deployment), the uncertainty in bed stress from equation (4) is only dependent on the uncertainty in friction velocity. The propagation of uncertainty from friction velocity to the bed stress is calculated according to

$$\Delta_{\tau_b} = 2\tau_b\frac{\Delta u_*}{u_*}, \quad (8)$$

where Δu_* is the error calculated using equation (7). Reasonable confidence intervals for shear velocity and bed stress calculations are contingent upon high coefficients of determination for the log layer fits.

[25] In this study, log layer fitting followed the methods discussed in *Lueck and Lu* [1997] and was applied to AWAC data collected during February 2011. For each profile, a least squares fit to the bottom bins of the profile (1.05 to 4.05 m) was first calculated. From the bottom bins, new fits were calculated adding one velocity bin each iteration until the profile extended to 25 m from the seabed. The log layer depth (z) was defined as the depth at which the highest R^2 value was identified. Only those fits with maximum R^2 exceeding 0.95 were retained. This most often was absent during transitions between flood and ebb tides, so data with near-bed currents below 0.5 m s^{-1} were not analyzed.

2.3.2. Reynolds Stress

[26] In a turbulent flow, the velocity is described by $(\overline{u_i} + u_i')$, where $\overline{u_i}$ is the mean velocity, u_i' is the velocity fluctuation, and the index (i) denotes the velocity component. The instantaneous kinematic stress, based on velocity fluctuations in the vertical and along channel flow, is written as $u'w'$, and is calculated as the covariance of the components. By assuming a constant stress layer, the bed stress is obtained from the Reynolds stress by

$$\tau_b = -\rho\overline{u'w'}, \quad (9)$$

where ρ is the fluid density. In general, Reynolds stress calculations are noisy because the variance of each flow component is large relative to the mean [*Gross and Nowell*, 1983]. Rigorous treatment of the Reynolds stress calculations and shear stress estimates is presented in both oceanographic and atmospheric literature [*Tennekes*, 1973; *Heathershaw*, 1979; *Gross and Nowell*, 1983; *Heathershaw and Thorne*, 1985; *Trowbridge et al.*, 1999; *Lu et al.*, 2000].

[27] Turbulent Reynolds stresses were calculated from ADV data for each 5 min interval directly from the covariance of along-channel and vertical velocity components according to equation (9). The correlation coefficient and coefficient of determination for each Reynolds stress calculation were calculated. An autocorrelation of the Reynolds stress was used to identify the decorrelation time scales, which were generally on the order of 1 sec. The number of degrees of freedom was calculated as the full sample length (256 sec) divided by the event duration (twice the decorrelation time) [*Gross and Nowell*, 1983]. The degrees of freedom, t-statistic, and R^2 value were used in equation (7) to calculate the uncertainty in the shear velocity which is propagated to the bed stress. To remove spurious data, when the relative Reynolds stress uncertainties exceeded 100% (data with low velocities when the variance of the velocities fluctuations was large relative to the mean velocity), the data were excluded from analysis. As for the log layer method, the excluded data were associated with the transition flows.

2.3.3. Inertial Dissipation

[28] Kolmogorov hypothesized large, turbulent eddies transfer energy to increasingly smaller eddies until viscous dissipation takes place at scales on the order of the Kolmogorov length. Although the largest scales of turbulence may not be isotropic, Kolmogorov noted that the energy cascade through the inertial subrange from the large, energy containing eddies to dissipation scales consists of isotropic turbulent eddies. For an isotropic turbulent energy cascade, the frequency spectrum of turbulent kinetic energy is described by

$$S(f) = \alpha\epsilon^{2/3}f^{-5/3}\left(\frac{\overline{u}}{2\pi}\right)^{2/3}, \quad (10)$$

where α is a constant taken to be 0.69 when using the vertical velocity spectrum, ϵ is the dissipation rate, f is the frequency, and $\overline{u}$ is the mean along-channel velocity at a given depth. Dissipation can be calculated by fitting a line to the portion of the turbulence spectrum with the $f^{-5/3}$ slope.

[29] For a fully developed, unstratified flow with negligible advection, the turbulent kinetic energy budget reduces to a balance between the production and dissipation of turbulence. This balance is described by

$$\epsilon = -\overline{u'w'}\frac{\partial u}{\partial z}, \quad (11)$$

where ϵ is the dissipation rate and $\overline{u'w'}$ is the kinematic stress. By assuming a constant stress layer and substituting the friction velocity for the kinematic stress ($u_*^2 = -\overline{u'w'}$), the bed stress can be found by

$$\tau_b = \rho(\epsilon\kappa z)^{2/3}, \quad (12)$$

where κ is the von Karmen constant.

[30] The dissipation of turbulent kinetic energy was calculated using the turbulent velocity spectrum for each ADV burst. Each 256 sec record was broken up into individual windows with 1024 data points and an overlap of 50%. After removing the mean, windows were multiplied by a Hann function and rescaled to preserve variance. An ensemble average of all windows in each burst produced the final spectrum. The first window was removed because the overlapping process resulted in zero padding of the first window. The resulting spectra have 40 degrees of freedom [*Priestley*, 1981]. The 95% confidence interval, obtained from a chi-squared distribution, is $0.61\,S(f) < S(f) < 1.48\,S(f)$ where $S(f)$ is the turbulence spectrum.

[31] The vertical velocity spectrum was used to estimate the dissipation rate of turbulent kinetic energy because the

ADV beam geometry resulted in less noise in the vertical direction. The vertical velocity spectrum was multiplied by $f^{5/3}$ to obtain a flat spectrum in the inertial subrange. The slope of the spectrum was calculated over a series of frequency ranges: 0.25–1, 0.5–2, 1–6, 4–8, 8–12, and 12–16 Hz. The fits for the frequency ranges contained either 25, 65, or 81 points. The frequency range with the minimum slope was defined as the inertial subrange. The dissipation was calculated by setting the mean value over this range equal to $\alpha\epsilon^{2/3}\left(\frac{\bar{u}}{2\pi}\right)^{2/3}$ and solving for ϵ. Uncertainties were calculated by finding the standard deviation and 95% confidence intervals for the spectrum values in the frequency range of the fit. The relative uncertainty bounds for the bed stress, obtained by propagating the uncertainty in the dissipation rate through equations (10) and (12), are

$$\Delta\tau_b = \sqrt{\frac{4\rho^2\kappa^2 z^2}{9\,(\kappa\epsilon z)^{2/3}}(\Delta\epsilon)^2}, \tag{13}$$

where the uncertainties of all of the variables, with the exception of the dissipation rate, are negligible.

[32] On the tripod, the ADV was deployed immediately adjacent to a second hydrophone shrouded in a shield intended to reduce measurements of flow-noise (10 cm diameter, 43.2 cm height). The sampling volume was approximately 15 cm from the flow shield. A projection of the wake in the direction of the flow revealed that when ebb velocities exceeded 0.5 m s^{-1}, the ADV sampling volume was immediately downstream of the flow shield. As a result, the measurements from the ADV during ebb tides may have been compromised by the wake and are not presented.

2.3.4. Drag Coefficients

[33] The drag coefficients for flood and ebb tides and their respective uncertainties were calculated by regressing the shear velocity versus the mean current squared. The regressions were performed in both log space and linear space. In linear scale calculations large shear velocities are emphasized whereas log scale calculations emphasize small shear velocities [*Lueck and Lu*, 1997]. For comparison, the drag coefficients were calculated for Reynolds stress and inertial dissipation techniques. For both techniques, equation (4) governs the relationship between the calculated bed stresses, shear velocities, and drag coefficients.

2.4. Acoustic Data Processing

[34] Acoustics data were processed using standard signal processing techniques. For the primary data set of February 2011, the digitized signals were converted to voltage and split into windows containing 2^{16} data points with a 50% overlap. For each window, the mean voltage was removed, a Hann function applied, and the signal scaled to preserve variance before applying a Fast Fourier Transform (FFT). Calibration curves were applied to convert voltage spectra to pressure spectra. Ensemble averages of the windowed pressure spectra were calculated to improve the underlying statistics in each 10 sec recording (ensemble size of 23, bandwidth of 1.2 Hz). The one-third octave band sound pressure levels (TOLs) [1–25 kHz center frequencies] were calculated by integrating under the spectra.

[35] The June–September 2012 data were processed in two ways to support the analysis of stationarity and intermittency. First, to produce spectrograms with high temporal resolution ($\Delta t \approx 0.025$ seconds), data were processed using 2^{12} data points (bandwidth of 19.5 Hz). Spectra and broadband sound pressure levels (2–20 kHz) were also calculated in 1 sec windows (ensemble size of 38). These data were used to highlight mobilization events in the direct vicinity of the hydrophones. Stationarity was investigated by subsampling each 55 sec recording to obtain five total signals (4 subsamples and the original). The subsampled signals were the first 1, 5, 10, and 30 sec of each recording. These four signals and the entire 55 sec recording were used to calculate the TOLs (ensemble sizes: 40, 196, 391, 1172, 2344). The resulting TOLs were used to compare the results of different duty cycles by subtracting the TOLs of the 55 sec recordings from those calculated using the 1, 5, 10, and 30 sec subsamples. A distribution of the results, using 0.5 decibel bins, was calculated for three different frequencies (4, 8, and 16 kHz) during all periods when sediment-generated noise occurs and in one velocity bin (ebb currents between 1.15–1.35 m s^{-1}).

2.4.1. Frequency Dependence of Sediment-Generated Noise

[36] The equivalent grain diameter for the particles in this study were calculated using the theoretical expression in the form of equation (3), based on a fit to equation (2), for site specific material properties. Available information about the composition of the seabed note a mix of plutonic and metamorphic rocks [*Greene*, 2011]. Using the material properties of basalt (ρ = 2500 kg m^{-3}, E = 60 GPa, and σ = 0.15) the theoretical centroid frequencies for equivalent grain sizes were related by

$$f_c = \frac{206}{D^{0.9}}. \tag{14}$$

[37] The resonant frequencies for equivalent grain sizes present at the site did not vary significantly from the results obtained for basalt if other possible material types were assumed. Specifically, the material properties of granite, rhyolite, quartize, gneiss, and slate all resulted in equivalent grain diameters within 15% of those obtained under an assumption of basalt for a given frequency. This difference was relatively small when compared to the distributions of grain sizes which spans nearly two orders of magnitude from coarse sand to cobbles.

2.4.2. Directionality

[38] The directionality of sound can be determined using cross-spectral methods. In an array, the phase (ϕ_{12}) relationship between two independent signals can be calculated when coherence (γ_{12}) values are statistically significant. The squared coherence is calculated by

$$\gamma_{12}^2 = \frac{|S_{12}(f)|^2}{S_{11}(f)S_{22}(f)}, \tag{15}$$

where S_{12} is the cross-spectrum, S_{11} is the autospectrum of the first signal, and S_{22} is the autospectrum of the second signal [*Priestley*, 1981]. Each component of equation (15), as well as the coincident and quadrature spectra, is calculated from the October 2011 drift study according to the previously identified signal processing techniques (i.e., windowing and averaging) prior to the calculation of the coherence. Data windows contained 2^{15} points with a 50% overlap, resulting in spectra with a bandwidth of 39.1 Hz. Processed data were used to calculate the phase lags between

the two hydrophones at frequencies of interest during strong currents to indicate whether the noise was generated above or below the hydrophones (section 2.4.2). Mean squared coherence was calculated for 10 sec sequences (ensemble size 180). Phase lags were calculated with respect to the deeper hydrophone such that a negative phase lag indicates noise generated below the array. The maximum uncertainty of the phase attributable to the DAQ, based on the sampling uncertainty, was less than 3° at the frequencies of interest.

[39] Confidence levels for coherence represent the lowest mean-squared coherence that is expected to occur randomly. *Thompson* [1979] calculated the significance of squared-coherence values and compared the results to Monte Carlo simulations. The work demonstrated that the confidence interval is related to the number of degrees of freedom in the calculations for the mean-squared coherence by

$$\gamma^2_{1-\alpha} = 1 - \alpha^{\left[\frac{2}{\nu-2}\right]}, \tag{16}$$

where $1 - \alpha$ is the confidence level and ν is the equivalent number of degrees of freedom for the cross-spectrum [*Priestley*, 1981, Table 6.2].

[40] The phase relationships between signals are calculated using coincident and quadrature spectra. The phase lag, as a function of frequency, between signal one and signal two is calculated by

$$\phi_{12}(f) = tan^{-1}\left(\frac{-Q_{12}(f)}{C_{12}(f)}\right), \tag{17}$$

where ϕ_{12} is the phase lag, Q_{12} is the quadspectrum, and C_{12} is the cospectrum [*Priestley*, 1981]. Phase lag estimates are suspect, although not necessarily incorrect, when squared-coherence does not exceed the desired confidence level.

[41] For sediment-generated noise and a vertical line array of two hydrophones measuring collisions directly in-line with the array (i.e., collisions directly below the hydrophones for a vertical array), the estimated phase lag between two measurements is related to the acoustic frequency (f), speed of sound (c), and the separation distance between the hydrophones (L). As frequency increases, the phase lag of the signal is expected to increase linearly for a localized source directly below the array. Under ideal conditions, the phase lag relationship, in degrees, for the vertical line array is described by

$$\tilde{\phi}_{12}(f) = 360\left(\frac{fL}{c}\right), \tag{18}$$

where $\tilde{\phi}$ denotes the idealized phase lag for a source directly below a vertical array. In practice, the incidence angle (the location of the source relative to the line array) and the orientation angle for a line array (i.e., angle from vertical) are important. In both cases, deviations from the ideal case reduce the measured phase lag relative to the idealized value.

2.4.3. Noise Level Regressions

[42] To assess the relationship between near-bed current velocities and sediment-generated noise, regressions were performed using terms developed from the one-third octave band sound pressure levels and the near-bed velocity cubed. The velocity-cubed metric was used because it provides a logical balance between the units of sound and velocity. Using the plane wave assumption, the TOLs can be easily converted to an acoustic intensity (i.e., power per unit area). Likewise, the velocity-cubed metric, normalized by an area of 1 m^2, can be readily interpreted as a rate of energy input (i.e., power) per unit area. Thus, the regression coefficients may be thought of as representing of the efficiency with which hydrodynamic power is converted to acoustic power through the mobilization of sediment. The final equations and units for the terms used in the regression are described by

$$P_{a,m} = 10\,log\left(10^{\frac{TOL_m}{10}}\frac{p_o^2}{\rho c}\right)\ [\text{dB re 1 W m}^{-2}], \tag{19}$$

$$P_h = \frac{\frac{1}{2}\rho U^3}{A}\ [\text{W m}^{-2}], \tag{20}$$

where $P_{a,m}$ is the acoustic power in the *mth* TOL, P_h is the near-bed hydrodynamic power, p_o is the underwater reference pressure (1μPa), ρ is the density (1024 kg m^{-3}), c is the sound speed (1490 m s^{-1}), U is the along-channel, near-bed, mean velocity, and A is the area (1 m^2). The regression, described by

$$P_{a,m} = a_m + b_m P_h, \tag{21}$$

provides the coefficients a_m and b_m, which may be conceptually thought of as the background noise intensity (y-intercept, dB re 1W m^{-2}) and the efficiency with which the power input to the seabed by currents is converted to sound (slope, dB re 1W m^{-2} per unit increase in near-bed hydrodynamic power). We note that this should be considered only a conceptual framework to give physical context to the regression coefficients since, for example, the power input to the seabed is likely related to U^3. One could construct a similar conceptual framework around a U^2 dependence on the basis of drag forces acting on the seabed. In practice, we found that the use of a U^3 versus U^2 has little effect on the statistical power of the derived regression coefficients.

[43] Prior to estimating the regression coefficients, Automatic Identification System data (section 2.5.1) were used to remove measurements with co-temporal vessel traffic within 10 km of the site. For the remaining data, mean measured TOLs were calculated in 0.1 m s^{-1} velocity bins. Only periods when TOLs exceed the quiescent mean ($\overline{TOL}$ for $|U| <$ 0.3 m s^{-1}) by 3 dB or more were used in the regression. A separate regression was performed for each one-third octave band. The lowest velocity bin in which the 3 dB increase was noted for each TOL was considered the critical velocity. This critical velocity was used to estimate the critical shear stress for mobilization of the equivalent grain sizes according to the inversion of the spectrum. It should be noted that defining the critical shear stress as the point at which TOLs have increased by 3 dB is inherently conservative. *Miller et al.* [1977] notes that the threshold should be defined as the conditions (bed stress) just lower than that which results in incipient motion. By relying on increases in sound intensity above ambient noise levels (which are attributed to other sources) to identify critical bed stresses, the thresholds reported here differ from established definitions. However, no other method to identify incipient motion is suitable for these indirect observations.

[44] To access the regression quality, the R^2 values are calculated fits to velocity bin-averaged TOLs according to equations (19)–(21). Similarly, near-bed currents were used to create a reconstruction predicted TOLs using the regression results according to equation (22). The R^2 values were then calculated using observed TOLs and the TOLs predicted from the regression coefficients. These R^2 values represent the degree to which mean noise levels in a one-third octave band were dependent on the near-bed currents. To qualitatively demonstrate this dependence, the regression coefficients were used to construct a 24-hour spectrogram of noise levels from 1-25 kHz. Using the regression, the output was converted to TOLs according to

$$TOL_m(t) = 10log_{10}\left(\frac{\rho c}{p_o^2}10^{\frac{a_m}{10}}\right) + \frac{1}{2}b_m\rho U^3 \quad \text{[dB re 1}\mu\text{Pa]}, \quad (22)$$

with terms as defined in equations (19)–(21). The regression coefficients were only applied to conditions when mean currents exceeded the critical values. When near-bed velocities were below the critical value, the TOL values were taken to be only the first term of equation (22) (i.e., mean ambient noise during weak currents).

2.5. Exclusion of Other Noise Sources

2.5.1. Vessel Noise

[45] While noise from vessel traffic is often considered at frequencies lower than those of interest for this study (i.e., < 1 kHz), *Bassett et al.* [2012] identifies vessel traffic noise as an important contributor to ambient noise at the frequencies considered in this study. Consequently, a field assessment of sediment-generated noise from a location with high vessel traffic density needs to exclude periods when vessel traffic might substantially contribute to ambient noise. An Automatic Identification System (AIS) was deployed at the Admiralty Head Lighthouse in Fort Casey State Park, less than 1 km from the site, to log real-time vessel traffic data. An AIS receiver (Comar AIS-2-USB) and data acquisition computer recorded incoming AIS strings and appended them with a timestamp using a Python script written to record and archive the data. Data were post-processed using a Python package (NOAA data version 0.43) [*Schwehr*, 2010]. This process converted raw AIS transmissions into ASCII format text.

[46] Vessel coordinates and speed over ground were extracted from each AIS string. The coordinates were used to calculate the radial distance from the vessel to the hydrophone. To prevent vessel noise from biasing analysis of sediment-generated noise, all recordings of ambient noise with an AIS transmitting vessel in transit (vessel speed > 0.05 m s^{-1}) within 10 km of the site were excluded. In addition, acoustic data were reviewed manually and recordings with signals consistent with vessel traffic were also removed. This can occur when vessels that do not consistently transmit AIS information, such as military vessels, transit the site. Due to low signal-to-noise ratios relative to flow-induced pseudosound, such events were difficult to identify during periods of strong currents and were not removed from the data set [*Bassett*, 2010]. As demonstrated in section 3.2, this should not have an impact on the results because peak levels from vessel noise are exceeded by sediment-generated noise at the frequencies under consideration during strong currents.

2.5.2. Pseudosound

[47] Hydrodynamic flow-noise, or pseudosound, is a result of turbulent pressure fluctuations measured by hydrophones. This non-propagating noise is a low-frequency phenomenon and should not be included in a discussion of ambient noise. Studies have reported flow-noise from oceanic turbulence at frequencies as high as 110 Hz [*Gobat and Grosenbaugh*, 1997]. In a series of papers on hydrodynamic flow-noise and wind screen noise, Strasberg noted that the frequency of noise generated by turbulent pressure fluctuations is related to the wavelengths of the spatial velocity fluctuations and the mean velocity [*Strasberg*, 1979, 1984, 1988]. The upper frequency limit for flow-noise is described by $f = |u|\,\eta_o^{-1}$, where u is the mean current and η_o is the Kolmorgorov microscale, the smallest scale that can occur before viscosity damps out the turbulent fluctuations. The microscales are related to the dissipation rate by $\eta_o = (\nu^3/\epsilon)^{0.25}$ where ν is the kinematic viscosity and ϵ is the dissipation rate. For an extreme example, a peak dissipation rate of 0.002 m^2 s^{-3}, consistent with previous findings at the site in this study [*Thomson et al.*, 2012] is used. This dissipation rate implies bed stresses on the order of 10 Pa and suggests a microscale of 0.2 mm. With near-bed currents on the order of 2 m s^{-1}, the peak at the site, the maximum theoretical frequency at which flow-noise is expected is approximately 10 kHz. However, when the size of the hydrophone element is larger than the turbulent microscales, as is the case in this extreme example where the hydrophone diameter (0.019 m) is nearly two orders of magnitude larger than the Komolgorov microscale, the signal of pseudosound at these frequencies will be attenuated. This attenuation is a result of phase changes across the hydrophone that cause the pressure differences to partially cancel [*Strasberg*, 1979, 1984], such that the measurable limit of flow-noise is lower than the theoretical maximum. For peak conditions, the scales of turbulence of the same size as the hydrophone would result in noise up to 100 Hz.

[48] The basic characteristics of the acoustic spectra during periods with strong currents suggest that flow-noise is not the source of the increases above 1 kHz. Figure2 includes an example spectrum from a period with a near-bed velocity of 1.6 m s^{-1}. Between 1–2 kHz noise levels in this example, and in general for periods with strong currents, are within the range of observed noise levels during slack tide conditions (section 3.2). Furthermore, above 1 kHz, the observed spectra diverge from the observed and expected "red" spectrum associated flow-noise. Given that the analysis in this study focuses on frequencies greater than 1 kHz, we conclude that pseudosound is not of primary importance in this study and is "masked" by propagating ambient noise in the frequency range of interest.

3. Results

[49] There is a strong dependence of observed noise levels on near-bed currents (Figure 3). The combination of acoustic and hydrodynamic measurements are used further to analyze the relationships between sediment-generated noise levels and the near-bed currents. As for the methods, hydrodynamic results precede acoustic results. Following the hydrodynamic results, sections discussing the directionality, intermittency, and stationarity of observed noise

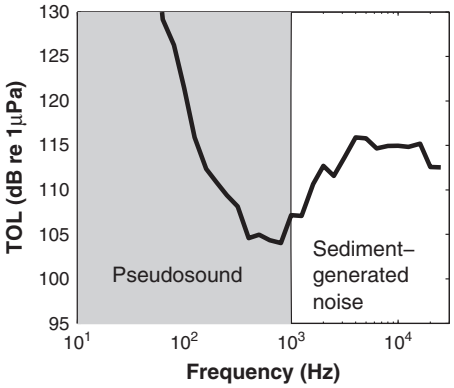

Figure 2. An example spectrum typical of acoustic measurements during strong currents. In this example with currents of 1.6 m s^{-1}, at frequencies below 1 kHz, the spectrum is "red" as expected for measurements of flow-noise. Above 1 kHz, the patterns are not consistent with flow-noise measurements, but rather with sediment-generated noise.

are presented along with a comparison of the observed noise measurements during comparable conditions during the three deployments. These relationships are summarized using a frequency dependent regression.

3.1. Hydrodynamics

[50] Bed stresses obtained via the log layer, Reynolds stress, and inertial dissipation techniques are plotted against the mean current for the bottom velocity bin (1.05 m) in Figure 4. Each measurement has unique error bars obtained according to the methodology discussed in section 2.3. For clarity, a single relative uncertainty representative of each method is included.

[51] A total of 75% of log layer fits meet the $R^2 > 0.95$ criterion. Periods when R^2 values are lower than 0.95 are typically associated with slack currents. When currents exceed 1 m s^{-1}, 99% of log layer fits have an R^2 value exceeding 0.95. No fits with R^2 values greater than 0.95 have fewer than 10 degrees of freedom (i.e., the log layer height is always at least 10 bins high). The propagation of the uncertainty to the shear stress calculation results in a maximum uncertainty of ±36%, although for currents greater than 1 m s^{-1}, the maximum uncertainty in shear stress is typically less than ±10%.

[52] Representative uncertainties for the Reynolds stress method are evaluated using the cumulative probability density of uncertainties (not shown). Fifty percent of uncertainties for this method are ±15% or less. A more conservative representative uncertainty for bed stresses of ±35%, the 95% value from the distribution, is chosen. For the inertial dissipation method, the representative uncertainty is chosen as the 95% value from a cumulative probability density function of relative uncertainties of the bed stress. The representative uncertainty is ±27%.

[53] Mean bed stresses, roughness length calculated by the log layer fits, and drag coefficients obtained using the Reynolds stress and inertial dissipation techniques are included for 0.25 m s^{-1} velocity bins in Table 2. The methods show good agreement and are in closest agreement when currents exceed 1 m s^{-1}. As discussed in section 3.2, these are the same periods in which significant increases of ambient noise are observed. Figure 4 also includes plots of the bed stresses estimated by the Reynolds stress method versus the inertial dissipation and log layer methods. During flood tides there is good agreement between the results for all three methods. During ebb tides the log layer and Reynolds stress methods agree well. As mentioned in section 2.3, the dissipation rate of turbulent kinetic energy during ebb currents are not included in Table 2 and Figure 4, because the measurements may have been compromised by the wake of another instrument. Bed stresses calculated by all methods are found to exceed 1 Pa at the site for currents greater than 0.5 m s^{-1}. Above 1 m s^{-1} mean bed stresses are approximately 5 Pa, and peak bed stresses exceed 20 Pa.

[54] The drag coefficient is calculated on both linear and log scales for comparison. Drag coefficients calculated using Reynolds stresses for the log and linear fits are indistinguishable with values of 0.0039 and 0.0045 for ebb and flood tides. The drag coefficients calculated using the Reynolds stress and inertial dissipation techniques during flood tides are comparable to values obtained at other sites with coarse-grained beds [*Williams et al.*, 1989; *Thorne et al.*, 1989; *Lueck and Lu*, 1997]. Based on the good agreement between the flood tide drag coefficients and measured data, the drag coefficient (C_D = 0.0044, linear scale) is applied later to calculate critical shear stresses.

3.2. Acoustics

3.2.1. Frequency Dependence of Sediment-Generated Noise

[55] When noise levels are considered across all stages of the tide, there are significant increases in noise levels relative to near-quiescent conditions above 1 kHz that are correlated with strong currents, as shown in Figure 5 for mean noise spectra in one-third octave bands in 0.2 m s^{-1} near-bed velocity bins. Previous analysis of data from the same site provide context for the increases in ambient noise attributed to the mobilization of the bed. *Bassett et al.* [2012] presents ambient noise levels, primarily associated with vessel traffic, for

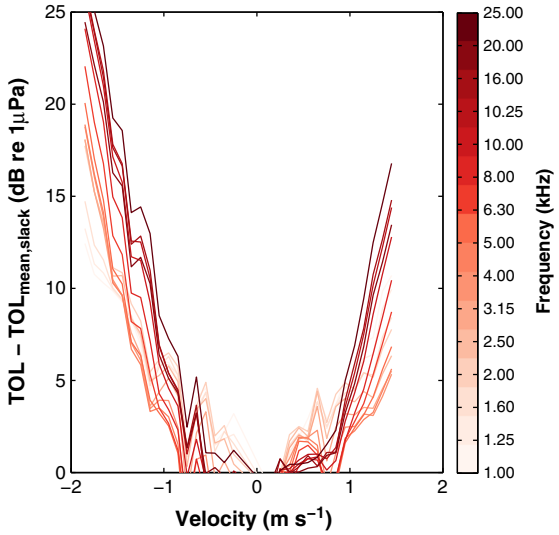

Figure 3. TOLs with the mean quiescent noise levels ($|U| <$ 0.3 m s^{-1}) subtracted versus near-bed current from 1 to 25 kHz.

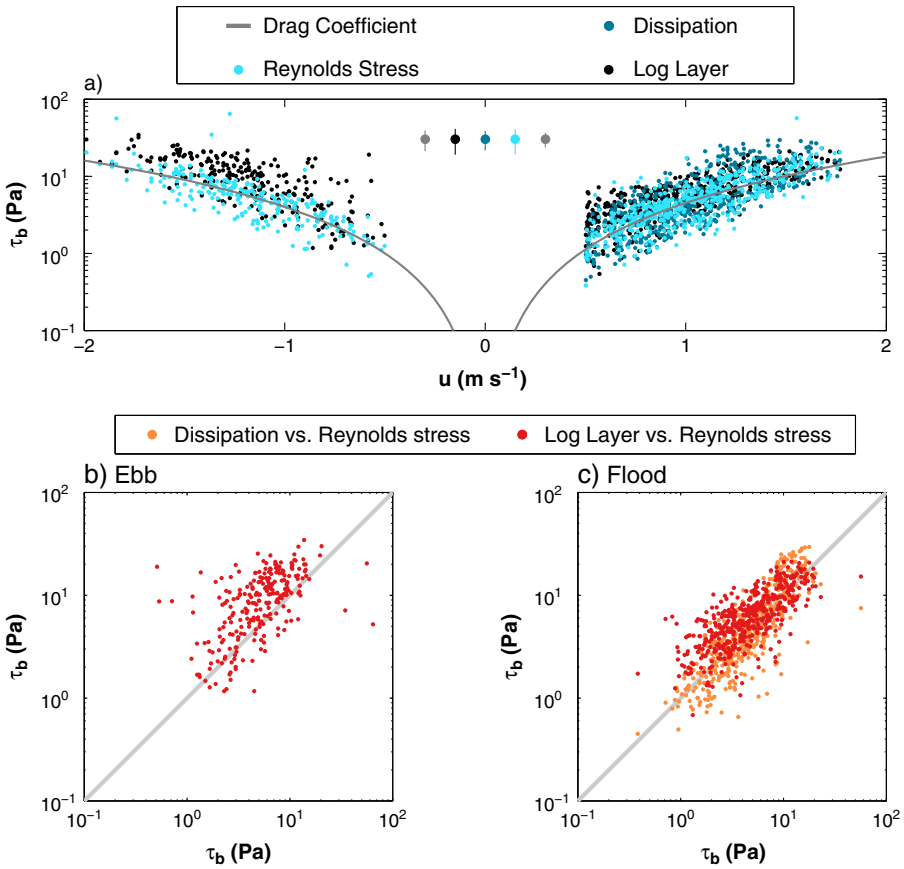

Figure 4. (a) Measured bed stresses versus mean velocity using inertial dissipation, Reynolds stress, log layer fits, and a drag coefficient (calculated from Reynolds stress estimate). Error bars highlight the representative 95% uncertainty values for each method. The drag coefficients and their uncertainties are calculated using a linear fit to Reynolds stress data (0.0039 for ebb tides and 0.0044 for flood tides, Table 2). (b) A comparison of bed stresses calculated by two methods for ebb tides. (c) A comparison of bed stresses calculated by three methods for flood tides.

Table 2. Mean Bed Stresses in 0.25 m s^{-1} Velocity Bins for Reynolds Stress, Inertial Dissipation, and Log Layer Fit Techniques, Roughness Length Calculated by Log Layer Fits, and Drag Coefficients

τ_b (Pa)	Velocity Bin (m s^{-1})	0–0.25	0.25–0.5	0.5–0.75	0.75–1.0	1.0–1.25	1.25–1.5	1.5–1.75	>1.75
Flood	Reynolds Stress	0.2	0.8	2.0	3.6	6.4	8.6	14.3	15.7
	Inertial Dissipation	0.1	0.5	1.8	3.2	6.4	10.8	14.3	13.5
	Log Layer	-	-	3.2	4.7	7.2	10.6	14.1	15.8
Ebb	Reynolds Stress	0.2	0.7	1.7	3.2	5.8	8.1	16.7	27.1
	Inertial Dissipation	-	-	-	-	-	-	-	-
	Log Layer	-	-	3.2	5.0	8.7	12.4	17.3	19.8

z_0 (m)	Velocity Bin (m s^{-1})	0–0.25	0.25–0.5	0.5–0.75	0.75–1.0	1.0–1.25	1.25–1.5	1.5–1.75	>1.75
Flood	Log Layer	-	-	0.018	0.008	0.007	0.007	0.005	0.005
Ebb	Log Layer	-	-	0.025	0.015	0.012	0.011	0.012	0.008

	Linear		Log	
C_D	Ebb	Flood	Ebb	Flood
Reynolds Stress	0.0039 ± 0.0011	0.0044 ± 0.0002	0.0039 ± 0.0010	0.0045 ± 0.0001
Inertial Dissipation	-	0.0033 ± 0.0001	-	0.0042 ± 0.0001

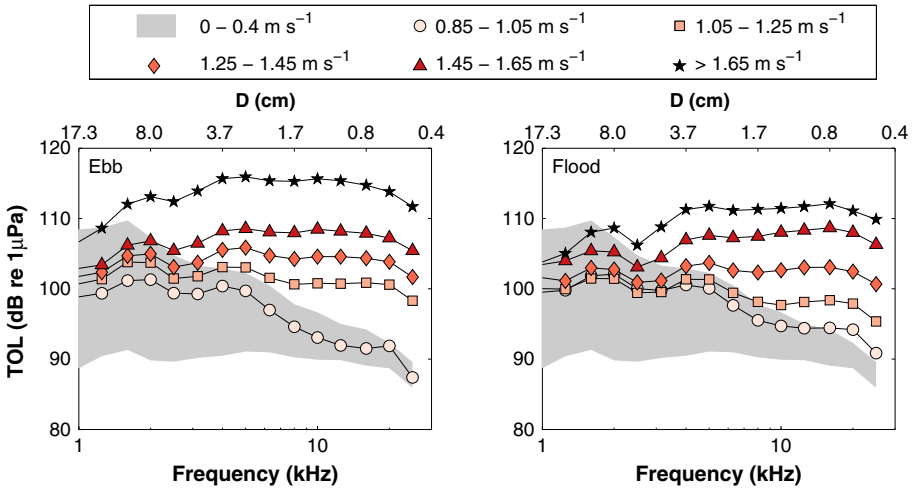

Figure 5. One-third octave band sound pressure levels versus frequency. The solid gray area highlights the 5% to 95% ambient noise statistics for currents less than 0.4 m s^{-1} [*Bassett et al.*, 2012]. Spectra are not shown for period with currents less than 0.85 m s^{-1} because segment-generated noise during these periods has no significant impact on noise levels. (a) Ensemble averaged acoustic spectra by velocity bin during flood tides. (b) Ensemble averaged acoustic spectra by velocity bin during ebb tides.

periods when near-bed currents (referenced to the bottom bin of current profiler) were less than 0.4 m s^{-1}. At the site, vessel presence is uncorrelated with the tide [*Bassett et al.*, 2012]. The shaded portions of Figure 5 highlight the 5% to 95% percentile spectra for periods with currents less than 0.4 m s^{-1} as presented in *Bassett et al.* [2012]. During the strongest currents, ambient noise levels above 1 kHz exceed the 95th percentile for quiescent conditions.

[56] These noise level increases are consistent with the production of sound by increasingly large sediment grains with stronger near-bed velocities. An estimate of the grain sizes that would contribute to noise level increases at a specific frequency is obtained by inverting equation (14). Each inversion is carried out on the lowest frequency that includes significant noise increases (+3 dB from quiescent conditions) for a given velocity. The equivalent grain sizes for the frequencies in the spectra (Figure 5), calculated using equation (14), are included on the secondary x-axis. Based on the inversion, the first increases in noise levels (i.e., at $f > 25$ kHz) are associated with grain sizes smaller than 1 cm and ebb currents of 0.65 m s^{-1}. As the currents and shear stresses increase, higher noise levels are attributed to grains as large as 17 cm (cobble). The greatest increases in noise intensity are associated with frequencies that, when inverted, would be categorized by the ROV survey as gravel (section 2.1). More modest increases also occur at frequencies that are associated with pebbles. As previously noted, a survey indicates that small cobbles, pebbles, and gravel are the primary grain sizes present on the seabed in the immediate vicinity of the site. Given the noted linear relationship between mobilized mass and sound intensity [*Thorne*, 1986b; *Thorne et al.*, 1989; *Williams et al.*, 1989; *Thorne*, 1990], the spectra suggest that mobile gravel is the most significant contributor to increased noise levels. As previously discussed, ROV survey notes indicate that larger sediments (boulder, cobble) are generally heavily encrusted while smaller sediments (gravel, pebble, and coarse sand) are not. This suggests that the modest increases in sound levels below 4 kHz are more likely caused by smaller, mobile grains impacting the larger, but immobile grains (e.g., cobbles).

[57] This hypothesis is supported by video data. In one particular sequence, a piece of mobilized gravel strikes a large pebble causing it to shift and strike an even larger pebble. In total, three pebbles shift as a result of the impact. Upon shifting, each pebble exposes a number of smaller gravel grains, comparable in size to the grain involved in the initial collision, which are rapidly entrained by the currents. A video of the described mobilization event, annotated snapshots from the video, and a spectrogram of the audio are provided as Supporting Information (online).

[58] As discussed in the methodology, the data used to identify the characteristics of sediment-generated noise were obtained during three deployments over a period of more than 18 months. The February 2011 and June–September 2012 sets both included fixed measurements 1 m above the seabed and the October 2011 drift measurements were taken at a depth of approximately 40 m (10–15 m above

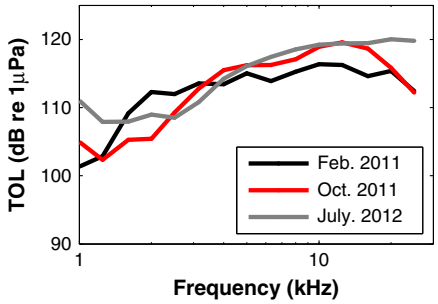

Figure 6. Observed one-third octave band sound pressure levels obtained during three deployments. The Feb 2011 and July 2012 recordings were obtained 1 m above the seabed and the Oct 2011 measurements were obtained 10–15 m above the bed while drifting.

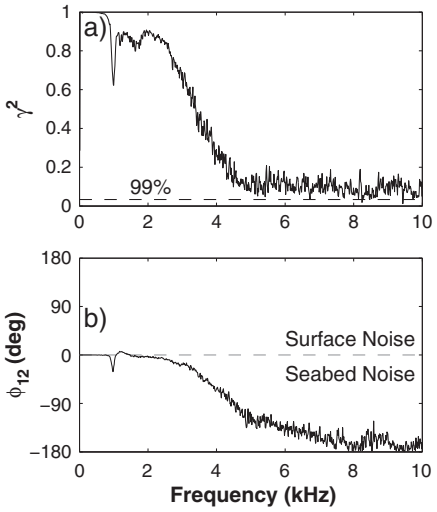

Figure 7. (a) Mean squared coherence versus frequency. Coherence values exceed the 99% confidence level below 10 kHz. (b) Phase lag versus frequency calculations. The dotted gray line separates the domains for surface and seabed generated noise. The spike at 1 kHz is associated with a peak of the ambient noise spectra from an unidentified source.

the seabed). Using velocity data from the Doppler profilers a period of strong, near-bed, ebb currents of approximately 1.65 m s^{-1} is identified in each of the data sets. Example acoustic spectra from these periods are included in Figure 6. The frequency content and amplitude of the observed noise in all three data sets are comparable under similar hydrodynamic conditions. When compared to other spectra in Figure 5, it is clear that the TOLs are typical of those that are only found during periods with strong near-bed currents. The similarities between the spectra suggest no significant changes in the composition of mobile particles at the site.

3.2.2. Directionality of Sediment-Generated Noise

[59] Vertical array results provide additional evidence that elevated noise levels are associated with sediment movement. Figure 7 includes plots of coherence and phase lag obtained using the cabled hydrophone array. At the time the data in Figure 7 were recorded, near-bed currents were 1.65 m s^{-1} (ebb tide). These currents would be expected to result in significant sediment-generated noise above 3 kHz (Figure 5). The depth of the hydrophones at the time of the recordings was 41.2 m (between 10 and 15 m above the seabed).

[60] For the entire frequency range in Figure 7 (0.02–10 kHz), mean square coherence levels exceed the 99% confidence levels. The increasing negative phase lag with frequency suggests that the seabed is the noise source for frequencies from 2 kHz to 10 kHz. Below 2 kHz, the dominant sound sources would likely be more distant sources (e.g., vessels) for which arrival angles are expected to be nearly horizontal (i.e., phase lag approaching 0°). The slope of the line above 2 kHz also indicates a mean phase lag associated with near vertical arrival angles. A similar pattern of phase lags with the expected phase wrapping occurs at higher frequencies, but above 10 kHz, the coherence levels do not exceed the 99% confidence level. Decreases in the coherence above 2 kHz may be attributable to the nonstationarity of the signal due to the intermittent nature of the sediment-generated noise, changing vessel position, or the diffuse nature of mobilization events on the seabed due to turbulence (as indicated by video observations). Although the precise location of the source of the noise cannot be determined by the array, the negative phase lag is not only consistent with a sound source originating from below the array, but the increasingly negative phase lag with frequency is also consistent with near-vertical arrival angles. Differences between the idealized phase lag for a source directly below the array and observed phase lag ($\tilde{\phi}$ and ϕ) may be attributed to a number of factors including the location of

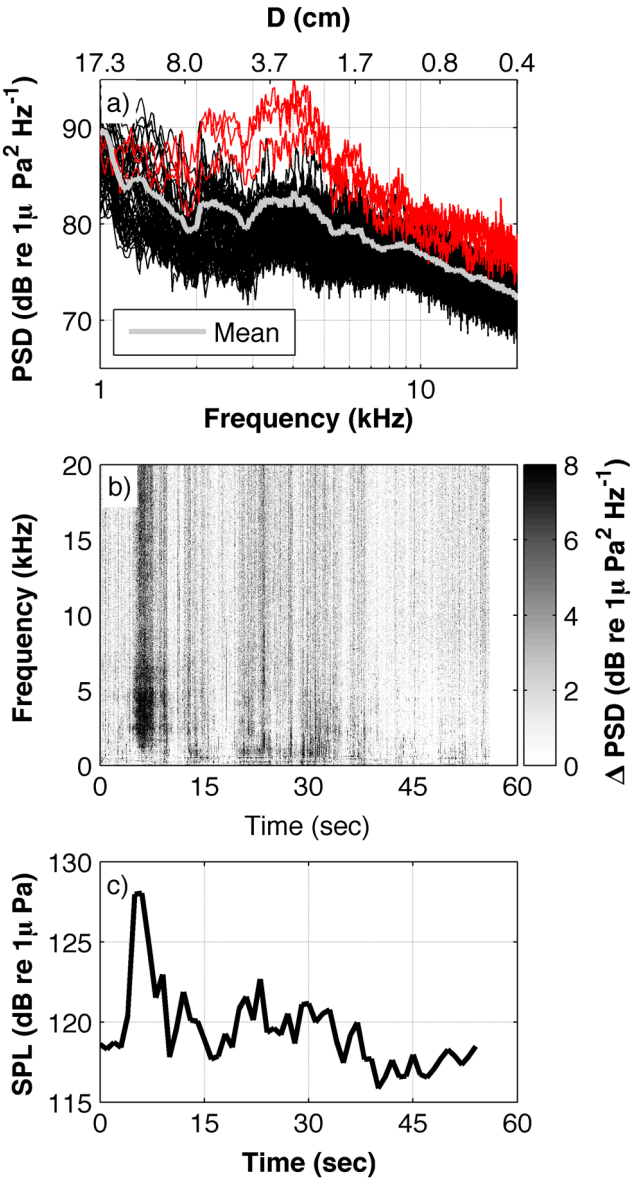

Figure 8. Example of intermittent acoustic data for a 55 sec recording with mean currents of 1.15 m s^{-1} (ebb) recorded on 27 July 2012. (a) One second average acoustic spectra (black), the spectra associated with the local mobilization event beginning at 5 sec in the recording (red), and the 55 sec average spectrum (gray). (b) Spectrogram with 1 min mean spectrum subtracted. (c). Time series of broadband SPLs (2–20 kHz).

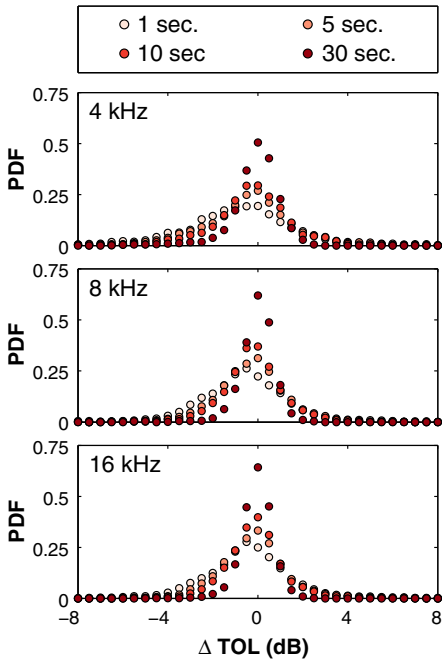

Figure 9. Probability distribution functions of the difference between 55 sec TOLs and 1, 5, 10, and 30 sec TOLs for ebb currents between 1.15 and 1.35 m s^{-1}. Other velocity bins and frequency bins are not shown but have similar distributions.

the noise sources on the seabed and off-vertical hydrophone orientation. Although there was no significant wire angle observed during the deployment, it is possible that vertical shear lower in the water column may have resulted in a horizontal displacement between the upper and lower hydrophones changing the vertical separation distance and the orientation angle of the line array resulting in a decreased phase lag.

3.2.3. Intermittency and Stationarity

[61] The sound produced by sediment grains shifting on the seabed is not continuous. That is, bed load transport is not sustained at a given location throughout the tidal cycle. The mean spectra are representative of characteristic noise levels integrated over an area of the seabed under different hydrodynamic conditions, but do not provide details about transient events. For example, a series of 1 sec average spectra, a spectrogram with the 55 sec mean spectrum subtracted, and a time-series of broadband (2–20 kHz) sound pressure levels, presented in Figure 8, show the dominant signal associated with a single local mobilization event. The peak intensities suggest that both the pebbles and gravel were mobilized. Manual review of the recorded audio reveals elevated noise levels attributable to sediment motion although the identification of individual events is generally not possible (i.e., the spectra in Figure 8 are representative of a minority of recordings when sediment generated noise is present). However, when localized events occur near the hydrophone, the identification of sound from individual events is possible. During these instances, the sound is similar to what one hears when gravel is poured over a pile of gravel. During these events, broadband sound pressure levels increase by up to 15 dB with energy contained in frequency bands between 1 and 30 kHz.

[62] As demonstrated in Figure 8, intermittent signals associated with highly localized mobilization events have the potential to impact sediment-generated noise statistics based on the averaging period or the duty cycle of the recording instrument. Figure 9 includes the probability distribution functions of the difference between TOLs calculated using 55 sec averages and those calculated using 1, 5, 10, and 30 sec averages for three frequencies (4, 8, and 16 kHz). For each frequency, the mean TOL is approximately the same (< 1 dB difference) regardless of the length of the recording. However, as is expected for a weakly stationary signal, in each case, the distribution is narrower for longer averaging periods.

3.3. Noise Level Regressions

[63] Regression statistics for the sound intensity versus near-bed hydrodynamic power per unit area are included in Table 3 for the velocity bin averaged acoustic data and for

Table 3. Results and Statistics for the Noise Versus Velocity-Cubed Regressions[a]

	Ebb						Flood					
f_c (kHz)	a_m	b_m	$\overline{u}_{cr}$ (m s^{-1})	R^2 Time Series	n	R^2 Bin Ave.	a_m	b_m	$\overline{u}_{cr}$ (m s^{-1})	R^2 Time Series	n	R^2 Bin Ave.
1	–85.4	0.0024	1.25	0.15	463	0.97	–87.6	0.0042	1.25	0.23	438	0.93
1.25	–85.1	0.0031	1.25	0.25	463	0.99	–88.4	0.0048	1.25	0.32	438	0.94
1.600	–83.5	0.0042	1.25	0.39	463	0.99	–87.7	0.0055	1.25	0.38	438	0.95
2.000	–83.6	0.0046	1.25	0.44	463	0.98	–87.9	0.0056	1.25	0.42	438	0.94
2.500	–86.1	0.0052	1.25	0.54	463	0.99	–89.3	0.0054	1.25	0.45	438	0.92
3.150	–86.1	0.0058	1.25	0.62	463	0.99	–89.9	0.0064	1.25	0.46	438	0.93
4.000	–84.5	0.0060	1.25	0.62	463	0.99	–88.0	0.0068	1.25	0.42	438	0.91
5.000	–84.9	0.0064	1.15	0.60	564	0.99	–86.6	0.0065	1.15	0.47	645	0.93
6.300	–86.6	0.0069	1.05	0.65	700	0.99	–88.9	0.0074	0.95	0.59	1049	0.96
8.000	–87.7	0.0075	0.95	0.67	782	0.98	–90.4	0.0082	0.85	0.70	1256	0.98
10.000	–88.2	0.0078	0.85	0.68	837	0.98	–91.1	0.0089	0.85	0.73	1256	0.98
12.500	–88.1	0.0076	0.85	0.62	837	0.98	–91.0	0.0091	0.85	0.70	1256	0.98
16.000	–88.1	0.0075	0.85	0.55	837	0.97	–90.8	0.0090	0.85	0.67	1256	0.98
20.000	–87.8	0.0069	0.85	0.52	837	0.97	–91.0	0.0088	0.85	0.67	1256	0.98
25.000	–91.6	0.0078	0.65	0.59	949	0.96	–95.2	0.0102	0.85	0.72	1256	0.97

[a]Coefficients a_m (ambient noise) and b_m (efficiency) correspond respectively to the y-intercept and slope of the acoustic intensity versus hydrodynamic power for one-third octave bands. R^2 values are calculated for the time series data with no vessels present using the coefficients from the velocity bin averaged regressions. The total number of points used to calculate raw R^2 values is n. The threshold for significant noise increases, +3 dB from mean slack tide conditions is $\overline{u}_{cr}$(m s^{-1}).

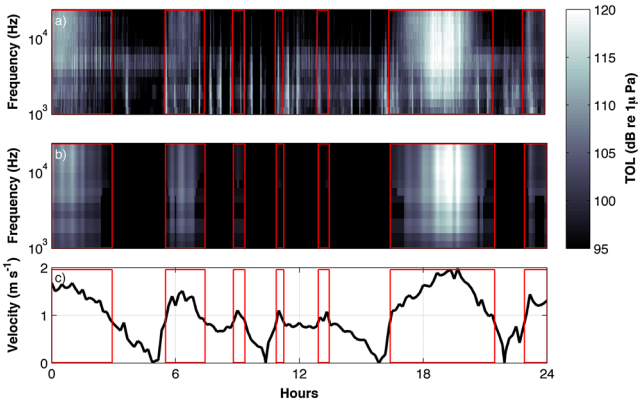

Figure 10. Comparison of observed noise levels and a time series constructed from the regressions coefficients for 17 February 2011. Periods with currents exceeding 1 m s^{-1} are highlighted. (a) Measured spectrogram. The regular increases in broadband noise levels during weak currents are a result of vessel traffic. (b) Spectrogram reconstructed using regression coefficients. (c) Near-bed currents.

the time series data using the regression coefficients obtained from the bin averaged data (note again that the bin averaged data are required to identify critical near-bed velocities). The regression coefficients suggest that, in the absence of sediment-generated noise, these frequency bands would be relatively quiet and that the conversion of hydrodynamic to acoustic power is inefficient. These are both physically realistic relations and consistent with the prior discussion. For bin-averaged data, the R^2 values for both flood and ebb currents exceed 0.9 for all frequency bands.

[64] The R^2 values for the unbinned time series data are lowest at the low frequencies, but still highly significant given the total number of data points included in the regressions. The source of the lower R^2 values, specifically at lower frequencies, can be explained by the low signal-to-noise ratio of sediment-generated noise to other ambient noise sources and the section on intermittency and stationarity (section 3.2.3). Especially below 4 kHz, noise levels during periods of strong currents fall within the range associated with quiescent conditions. As such, scatter in the data at these frequencies may be in part attributed to other noise sources. In all frequency bands, there is also more scatter in the acoustic data during low currents.

[65] Based on the method, the onset of noise level increases is correlated with bed stresses on the order of 3 Pa. In general, the regression slope coefficient increases with frequency, suggesting that hydrodynamic power is more efficiently converted to acoustic power for small grain sizes. Just as mean shear stresses in a velocity bin vary between flood and ebb currents, noise levels and the efficiencies also vary between flood and ebb tides. The ebb efficiencies, converted to an approximate noise level increase in 0.1 m s^{-1} bins, range from approximately 0.9 (1 kHz) to 3 dB (25 kHz) per 0.1 m s^{-1} increase in the near-bed velocity. During flood tides, the comparable coefficients are 1.5 (1 kHz) to 3.6 dB (25 kHz) per 0.1 m s^{-1} increase in the near-bed velocity.

[66] To provide a qualitative example of the predictive value of the regression coefficients, a time series of TOLs and currents is included in Figure 10 for a 24 h period. Both regression coefficients are only applied to TOLs when the mean currents exceed the critical velocity (Table 3). Vessel traffic, which is not represented using the regressions, regularly increases TOLs in all measured frequency bands (as previously discussed, the regression values are derived from observations without vessel traffic). During strong currents, there is good agreement in received levels across all frequency bands included in the regressions. This agreement demonstrates that sediment-generated noise levels at the sites are highly predictable from the near-bed velocity, once site-specific regression coefficients have been obtained. At this site, strong spatial gradients result in significant reductions in currents at scales on the order of 100s of meters [*Palodichuk et al.*, 2013]. As a result, sediment-generated noise levels are expected to change at comparable length scales.

4. Discussion

[67] The results presented here demonstrate a rich relationship between hydrodynamics, the physics of incipient motion and mobilization of heterogeneous, coarse-grained beds, and ambient noise in high-energy environments. As demonstrated in Figure 5, sediment-generated noise is a significant source of ambient noise at this location. The intensity and regularity of sediment-generated noise is dependent on hydrodynamic conditions and seabed composition. If conditions regularly mobilize the bed, sediment-generated noise can contribute significantly to ambient noise over a broad frequency range related to the local composition of the seabed.

4.1. Bed Stress and Sediment Mobilization

[68] The shear stresses at which increases in ambient noise are attributed to sediment-generated noise are lower than previous estimates discussed in section 1. Again, we note that the thresholds defined in this study are based on increases in TOLs, which require regular mobilizations or collisions between grains. In this study, noise levels for equivalent grains size up to 6 cm (f > 2.5 kHz) increase with shear stresses greater than 7 Pa. By contrast, comparable values were noted by *Thorne et al.* [1989] for sand and gravel in a tidal channel and by *Miller et al.* [1977] for 1 cm equivalent grain sizes in experimental work. A comparison between critical shear velocities (u_{*c}) calculated for site specific data, the Shield's parameter (assuming Θ_c = 0.06), and *Hammond et al.* [1984] are included in Figure 11. The site specific critical shear stresses were calculated assuming a drag coefficient of 0.0044 (section 3.1) and the critical velocity thresholds included in Table 3. The critical shear stresses for all calculated grain sizes are lower than the critical values using the Shields parameter and *Hammond et al.* [1984].

[69] The referenced thresholds for sediment movement, described in *Miller et al.* [1977], which covers literature dating back to *Shields* [1936], are derived from simplified experimental studies intended to reduce scatter in the data sets. Amongst the common design parameters are unidirectional flows, flumes with parallel sidewalls, and beds consisting of rounded, uniformly sized grains. Lower observed

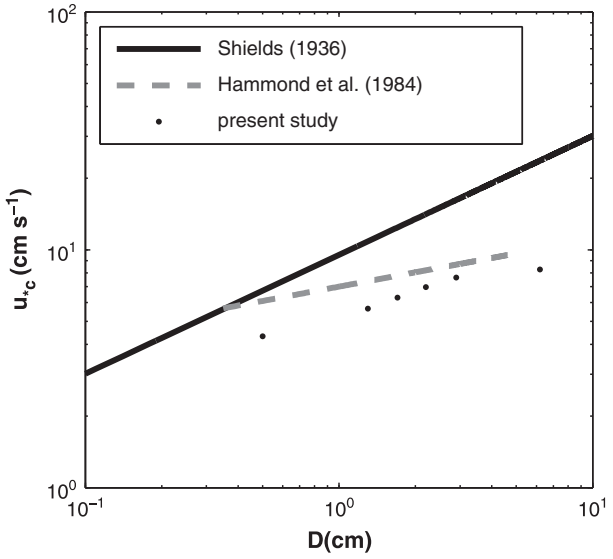

Figure 11. Critical shear velocities versus equivalent grain diameter.

thresholds for larger grains in natural environments can be related, in part, to differences in hydrodynamics conditions (e.g., turbulence), bed roughness, grain size distribution, grain spacing, and grain protrusion into the flow. In a heterogeneous bed, larger grain sizes carry a disproportionately large fraction of bed stress which, in turn, leads to mobilization at lower bed stresses than those that would be expected for a uniform bed consisting of smaller grains [*Hammond et al.*, 1984]. Turbulent bursts, particularly events with positive along-channel velocity fluctuations, have been found to be related to the most significant transport events [*Heathershaw and Thorne*, 1985; *Thorne et al.*, 1989]. Lower turbulence in controlled laboratory experiments may also contribute to differences between mean thresholds in the laboratory and the marine environment.

4.2. Intermittency and Stationarity

[70] During an observation period, sediment-generated noise levels are not constant. When turbulent bursts cause the motion of larger grains, more grains are exposed to entrainment. This process can result in sudden transport of many smaller, less exposed particles [*Hammond et al.*, 1984; *Heathershaw and Thorne*, 1985]. Transport events have also been attributed to significant intermittent increases in bed stresses above the mean that are associated with turbulence. Mean recorded sound intensities are a result of the summation of received levels from individual events in surrounding areas of the seabed. This summation represents the average conditions at the site. When a mobilization event occurs in the immediate vicinity of the hydrophone, integrated received levels from the seabed are dominated by the mobilization event closest to the hydrophone. While unpredictable, these intermittent events do not have a significant impact on the overall predictability of noise levels from sediment transport, as shown in section 3.3. This result is attributed to the cumulative nature of noise measurements near the seabed. That is, although transport events are intermittent for these coarse grains, mobilization events distributed over the seabed result in predictable noise levels. Based on the relationship of TOLs to near-bed currents, duty cycling and averaging periods can be increased to reduce scatter but should not exceed the time scales over which tidal currents can be considered stationary (approximately 5 min at this site).

4.3. Masking of Other Noise Sources

[71] Sediment-generated noise at the study site in Admiralty Inlet is the most significant contributor to ambient noise above 2 kHz during periods of strong currents. From 2 to 30 kHz, sediment-generated noise is sufficiently loud to regularly mask all other common noise sources, including rain, breaking waves, and vessel traffic in the same frequency range. The masking potential of sediment-generated noise at the site is particularly striking above 4 kHz. These noise levels exceed the 95% noise levels during quiescent conditions, which are attributed primarily to vessel traffic by up to 20 dB.

[72] From a practical standpoint, the limitations placed on passive acoustic studies due to sediment-generated noise are mostly limited to frequencies greater than 2 kHz. In highly energetic coastal environments, this noise source could reduce the effective range of passive acoustic monitoring techniques. For example, sediment-generated noise overlaps with higher frequency components of vessel traffic noise that are often neglected in anthropogenic noise studies. In coastal environments, these contributions to anthropogenic noise can be significant [*Bassett et al.*, 2012].

[73] There is growing interest in developing tidal energy projects in energetic coastal environments. In these environments, sediment-generated noise may be common, emphasizing the need to better understand sediment-generated noise and its relevance to monitoring anthropogenic and biological noise sources. As a practical example, echolocation clicks of mid- and high-frequency cetaceans overlap with the frequencies of sediment-generated noise from coarse and fined grained sediments (1 kHz $< f <$ 200 kHz). Sediment-generated noise at these frequencies can be recorded by echolocation click detectors tuned to these frequencies (e.g., Chelonia C-POD) complicating biological assessments using these instruments.

4.4. Applicability to Other Sites

[74] Highly energetic sites such as the one discussed here represent a very small subset of coastal environments. Although research in such environments has resulted in a limited body of literature on the subject, we expect that high levels of ambient noise due to bed load transport are common in comparable areas. Sediment-generated noise from the resuspension and transport of sediments by surface waves in shallow waters may also be common over a wider geographic range.

[75] Sediment-generated noise is highly dependent on hydrodynamic conditions and seabed composition, limiting the direct application of results presented here to other sites. Nonetheless, a series of basic conclusions can be drawn with respect to sediment-generated noise. In general, sites with bed stresses that are sufficiently large to mobilize coarse grained sediments are unlikely to have significant amounts of exposed fine grain sediments (i.e., sand and clay) due to winnowing of these constituents. As a result, at sites with comparable hydrodynamic conditions, sediment-generated

noise is unlikely to be significant at high frequencies ($f > 50$ kHz, $D \approx 0.1$ cm, the upper limit for coarse sand) except in the cases of energetic estuaries with large suspended sediment loads from local inflows. More energetic sites are likely to produce noise at lower frequencies, unless scoured to bedrock, because larger shear stresses can support the motion of larger grain sizes.

5. Conclusion

[76] Analysis of hydrodynamic and acoustic measurements from a site in Admiralty Inlet, Puget Sound, WA (USA) suggests that sediment-generated noise is the dominant noise source between 1 and 30 kHz during periods of strong currents. Peak sediment-generated noise levels from 4 to 20 kHz are associated with mobile gravel and pebbles. Sediment-generated noise levels in one-third octave bands exceed noise levels attributed to vessel noise by up to 20 dB. Equivalent grain sizes, estimated by inverting the acoustic spectra associated with sediment-generated noise, are in agreement with the known distribution of grain sizes present at the site. Three methods of calculating the bed stress show good agreement for periods of strong currents. Using increases in noise levels at different frequencies, critical shear stresses for different grain sizes are estimated and found to be lower than laboratory studies despite the use of a more conservative definition of critical shear stress. Regressions of the sound intensity versus the near-bed hydrodynamic power per unit area show that noise levels are predictable and that the largest increases in noise levels are associated with smaller grains (higher frequencies). Localized, intermittent events can increase recorded noise levels by more than 10 dB over a period of seconds. Due to such events, the distribution of TOLs recorded in a velocity bin is narrower for longer recording periods, as long as near-bed velocities can still be considered stationary.

[77] **Acknowledgments.** Thanks to field engineers Joe Talbert and Alex deKlerk for the successful recoveries and deployments of the tripods. Many thanks to Capt. Andy Reay-Ellers, the captain of the R/V Jack Robertson, Andrea Ogston, Chris Chickadel, Sarah Giddings, and Michelle Hickner. We also thank the three anonymous reviewers for their helpful comments on the manuscript. Snohomish Public Utility District's interest in tidal energy was the motivation for studying ambient noise at the site. Washington State Parks allowed for the placement of the AIS system on Admiralty Head Lighthouse. Funding provided by U.S. Department of Energy award DE-EE0002654. Student support was provided to Christopher Bassett by National Science Foundation award DGE-0718124.

References

Bassett, C. (2010), Underwater ambient noise at a proposed tidal energy site in Puget Sound, Master's thesis, University of Washington.

Bassett, C., B. Polagye, M. Holt, and J. Thomson (2012), A vessel noise budget for Admiralty Inlet, Puget Sound, Washington (USA), *J. Acoust. Soc. Am.*, *132*(6), 3706–3719, doi:10.1121/1.4763548.

Brumley, B., R. Cabrera, K. Deines, and E. Terray (1991), Performance of a broad-band acoustic doppler current profiler, *IEEE J. Ocean. Eng.*, *16*(4), 402–407, doi:10.1109/48.90905.

Diplas, P., C. Dancey, A. Celik, M. Valyrakis, K. Greer, and T. Akar (2008), The role of impulse on the initiation of particle movement under turbulent flow conditions, *Science*, *322*(5902), 717–720, doi:10.1126/science.1158954.

Gobat, J. I., and M. Grosenbaugh (1997), Modeling the mechanical and flow-induced noise on the surface suspended acoustic receiver, 748–754, IEEE Oceans. doi:10.1109/OCEANS.1997.624086.

Goring, D., and V. Nikora (2002), Despiking acoustic doppler velocimeter data, *J. Hydraul. Eng.*, *128*(1), 117–126, doi:10.1061/(ASCE)0733-9429(2002)128:1(117).

Grant, W., A. Williams III, and S. Glenn (1984), Bottom stress estimates and their prediction on the Northern California continental shelf during CODE-1: The importance of wave-current interaction, *J. Phys. Oceanogr.*, *14*(3), 506–526, doi:10.1175/1520-0485(1984)014<0506:BSEATP>2.0.CO;2.

Green, M. (1992), Spectral estimates of bed shear stress at subcritical reynolds numbers in a tidal boundary layer, *J. Phys. Oceanogr.*, *22*(8), 903–917, doi:10.1175/1520-0485(1992)022<0903:SEOBSS>2.0.CO;2.

Greene, C. R., Jr., and S. Moore (1995), Man-made noise, in *Marine Mammals and Noise*, pp. 101–158, Academic Press, San Diego.

Greene, H., (2011), Habitat characterization of the SnoPUD turbine site—Admiralty Head, Washington State, *Tech. Rep.*, Sound and Sea Technology.

Gross, T., and A. Nowell (1983), Mean flow and turbulence scaling in a tidal boundary layer, *Cont. Shelf Res.*, *2*(2-3), 109–126, doi:10.1016/0278-4343(83)90011-0.

Hammond, F. D. C., A. D. Heathershaw, and D. N. Langhorne (1984), A comparison between Shields' threshold criterion and the movement of loosely packed gravel in a tidal channel, *Sedimentology*, *31*, 51–62, doi:10.1111/j.1365-3091.1984.tb00722.

Harden Jones, F., and R. Mitson (1982), The movement of noisy sandwaves in the Strait of Dover, *ICES J. Mar. Sci.*, *40*(1), 53–61, doi:10.1093/icesjms/40.1.53.

Heathershaw, A. (1979), The turbulent structure of the bottom boundary layer in a tidal channel, *Geophys. J. R. Astron. Soc.*, *58*, 395–430, doi:10.1111/j.1365-246X.1979.tb01032.X.

Heathershaw, A. D., and P. D. Thorne (1985), Sea-bed noises reveal role of turbulent bursting phenomenon in sediment transport by tidal currents, *Nature*, *316*(6026), 339–342, doi:10.1038/316339a0.

Lee, H., and S. Balachandar (2012), Critical shear stress for incipient motion of a particle on a rough bed, *J. Geophys. Res.*, *117*(F01026), 1–19, doi:10.1029/2011JF002208.

Lu, Y., R. Lueck, and D. Huang (2000), Turbulence characteristics in a tidal channel, *J. Phys. Oceanogr.*, *30*, 855–867, doi:10.1175/1520-0485(2000)030<0855:TCIATC>2.0.CO;2.

Lueck, R., and Y. Lu (1997), The logarithmic layer in a tidal channel, *Cont. Shelf Res.*, *17*(14), 1785–1801, doi:10.1016/S0278-4343(97)00049-6.

Ma, B., J. Nystuen, and R.-C. Lien (2005), Prediction of underwater sound levels from rain and wind, *J. Acoust. Soc. Am.*, *117*(6), 3555–3565, doi:10.1121/1.1910283.

Mason, T., D. Priestley, and D. Reeve (2007), Monitoring near-shore shingle transport under waves using a passive acoustic technique, *J. Acoust. Soc. Am.*, *122*(2), 737–746, doi:10.1121/1.2747196.

Mellen, R. (1952), The thermal-noise limit in the detection of underwater acoustic signals, *J. Acoust. Soc. Am.*, *24*(5), 478–480, doi:10.1121/1.1906924.

Miller, M., I. McCave, and P. Komar (1977), Threshold of sediment motion under unidirectional currents, *Sedimentology*, *24*(4), 507–527, doi:10.1111/j.1365-3091.1977.tb00136.X.

Mori, N., T. Suzuki, and S. Kakuno (2007), Noise of acoustic Doppler velocimeter data in bubbly flows, *J. Eng. Mech.*, *133*(1), 122–125, doi:10.1061/(ASCE)0733-9399(2007)133:1(122).

Nystuen, J., and H. Selsor (1997), Weather classification using passive acoustic drifters, *J. Atmos. Oceanic Technol.*, *14*, 656–666, doi:10.1175/1520-0426(1997)014<0656:WCUPAD>2.0.CO;2 .

Polagye, B., and J. Thomson (2013), Tidal energy resource characterization: Methodology and field study in Admiralty Inlet, Puget Sound, US, *IMechE, Part A: J. Power and Energy,* doi:10.1177/0957650912470081.

Polagye, B., B. Van Cleve, A. Copping, and K. Kirkendall, (2011), Environmental effects of tidal energy development, *Tech. Rep.*, 186 p, U.S. Dept. Commerce, NOAA Tech. Memo. NMFS F/SPO-116.

Palodichuk, M., B. Polagye, and J. Thomson (2013), Resource mapping at tidal energy sites, *J. Ocean. Eng.*, doi:10.1109/JOE.2012.2227578.

Priestley, M. (1981), *Spectral Analysis and Time Series*, 467, 660–661, Academic Press, London.

Schwehr, K. (2010), Python software for processing ais data. v0.43.

Shields, A. (1936), Application of similarity principles and turbulence research to bedload movement, Translated from Anwendung der Achnichkeits Geschiebebewegung, in *Mitt. Preuss. VersAnst. Wasserb. Schiftb.*, edited by W. D. Ott, and J. C. von Vcheten, vol. 167, 36 p., Publ. Calif. Inst. Technol. Hydrodyn. Lab.

Snohomish PUD, (2012), Admiralty Inlet pilot tidal project, FERC project no. 12690, *Tech. Rep.*, Public Utility District No. 1 of Snohomish County.

Strasberg, M. (1984), *Adaptive Methods in Underwater Acoustics*, 125–143, Reidel, Boston, MA.

Strasberg, M. (1988), Dimensional analysis of windscreen noise, *J. Acoust. Soc. Am.*, *83*(2), 544–548, doi:10.1121/1.396148.

Strasberg, N. (1979), Nonacoustic noise interference in measurements of infrasonic ambient noise, *J. Acoust. Soc. Am.*, *66*(5), 1487–1493, doi: 10.1121/1.383543.

Tennekes, H. (1973), The logarithmic wind profile, *J. Atmos. Sci.*, *30*, 234–238, doi:10.1175/1520-0469(1973)030<0234:TLWP>2.0.CO;2.

Thompson, R. O. (1979), Coherence significance levels, *J. of Atmos. Sci.*, *36*, 2020–2021, doi:10.1175/1520-0469(1979)036<2020:CSL>2.0.CO;2.

Thomson, J., B. Polagye, V. Durgesh, and M. Richmond (2012), Measurements of turbulence at two tidal energy sites in Puget Sound, WA (USA), *IEEE J. Ocean. Eng.*, *37*(3), 363–374, doi:10.1109/JOE.2012.2191656.

Thorne, P. (1985), The measurement of acoustic noise generated by moving artificial sediments, *J. Acoust. Soc. Am.*, *78*(3), 1013–1023, doi: 10.1121/1.393018.

Thorne, P. (1986a), Laboratory and marine measurements on the acoustic detection of sediment transport, *J. Acoust. Soc. Am.*, *80*(3), 899–910, doi: 10.1121/1.393913.

Thorne, P. (1986b), An intercomparison between visual and acoustic detection of seabed gravel movement, *Mar. Geol.*, *72*, 11–31, doi: 10.1016/0025-3227(86)90096-4.

Thorne, P. D., J. J. Williams, and A. D. Heathershaw (1989), In situ acoustic measurements of marine gravel threshold and transport, *Sedimentology*, *36*, 61–74, doi:10.1111/j.1365-3091.1989.tb00820.X.

Thorne, P. (1990), Seabed generation of ambient noise, *J. Acoust. Soc. Am.*, *87*(1), 149–153, doi:10.1121/1.399307.

Trowbridge, J., W. Geyer, M. Bowen, and A. Williams III (1999), Near-bottom turbulence measurements in a partially mixed estuary: Turbulent energy balance, velocity structure, and along-channel momentum balance, *J. Phys. Oceanogr.*, *29* (2), 3056–3072, doi:10.1175/1520-0485(1999)029<3056:NBTMIA>2.0.CO;2.

Voglis, G., and J. Cook (1970), A new source of acoustic noise observed in the North Sea, *Ultrasonics*, *8*, 100–101, doi:10.1016/0041-624X(70)90049-1.

Wentworth, C. K. (1922), A scale of grade and class terms for clastic sediments, *J. Geol.*, *30*(5), 377–392.

Wenz, G. (1962), Acoustic ambient noise in the ocean: Spectra and sources, *J. Acoust. Soc. Am.*, *34*(12), 1936–1956, doi:10.1121/1.1909155.

Williams, J., P. Thorne, and A. Heathershaw (1989), Measurements of turbulence in the benthic boundary layer over a gravel bed, *Sedimentology*, *36*, 959–971, doi:10.1111/j.1365-3091.1989.tb01533.X.